Structural distortion and magnetism in transition metal oxides: crucial roles of orbital degrees of freedom

2002 J. Phys.: Condens. Matter 14 3001

(http://iopscience.iop.org/0953-8984/14/11/312)

INSTITUTE OF PHYSICS PUBLISHING JOURNAL OF PHYSICS: CONDENSED MATTER

J. Phys.: Condens. Matter **14** (2002) 3001–3014 PII: S0953-8984(02)30744-6

Structural distortion and magnetism in transition metal oxides: crucial roles of orbital degrees of freedom

Zhong Fang[1] **and Kiyoyuki Terakura**[2,3]

[1] Joint Research Center for Atom Technology (JRCAT), Angstrom Technology Partnership (ATP), Central 4, 1-1-1 Higashi, Tsukuba, Ibaraki 305-0046, Japan
[2] Joint Research Center for Atom Technology (JRCAT), National Institute of Advanced Industrial Science and Technology (AIST), Central 4, 1-1-1 Higashi, Tsukuba, Ibaraki 305-8562, Japan
[3] Research Institute for Computational Sciences (RICS), AIST, Central 2, 1-1-1 Umezono, Tsukuba, Ibaraki 305-8568, Japan

Received 9 November 2001, in final form 4 January 2002
Published 8 March 2002
Online at stacks.iop.org/JPhysCM/14/3001

Abstract

A characteristic feature of the physics in transition-metal oxides is that the charge, spin, and lattice degrees of freedom are strongly coupled. The key to understanding these strong mutual couplings is the orbital degree of freedom (ODF), which plays a crucial role in controlling the phases and various physical properties. We have been working on TMO extensively in recent years. Examples are FeO and MnO, $La_{1-x}Sr_xMnO_3$, $Ca_{2-x}Sr_xRuO_4$, Sr_2FeMoO_6, and $SrTiO_3$, not only for the bulk but also for the surfaces. A review will be given in this article, with concentration on the strong coupling between the structural distortion and the magnetism mediated by ODF. Most of the studies were conducted by our STATE (simulational tool for atom technology) code, which is particularly designed for the transition-metal systems. Some particular aspects of STATE code, such as LDA + U method and virtual crystal approximation, will be also discussed.

(Some figures in this article are in colour only in the electronic version)

1. Introduction

The transition-metal oxides (TMO) which form an important category of materials in fundamental physics as well as in technological applications have been attracting intense attention from the condensed matter community [1]. They exhibit a rich variety of structural, magnetic, transport, and optical properties. For example, ferroelectricity of titanates and high T_c superconductivity of cuprates have been extensively studied and widely used in practice. More recently, the negative colossal magnetoresistance (CMR, i.e., 'more than giant' decrease of resistivity on application of magnetic field) in manganites [2, 3] and the unconventional

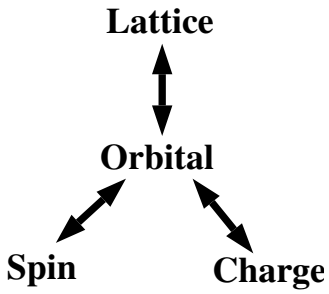

Figure 1. A schematic description for the strong couplings among some degrees of freedom existing in TMO. The ODF plays crucial roles in mediating these couplings.

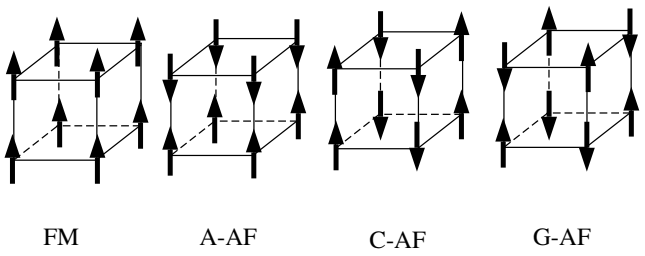

Figure 2. Various magnetic structures are schematically shown. From left to right, FM, A-type antiferromagnetic (A–AF) and so on.

spin-triplet p-wave superconductivity in ruthernates [4] set up additional challenges. All these physical properties can be controlled in various ways: ionic radii, electron or hole doping, magnetic or electric field, temperature, pressure, photoexcitation, and so on, providing possibility of wide practical applications.

It is interesting to note that the basic concepts needed to understand various phenomena are mostly rather old. For example, double exchange (DE) [5], super exchange (SE) [6], cooperative Jahn–Teller (JT) effect [7] and dynamical JT effect [8–10] form a basic set of concepts associated with the CMR effect in doped manganites. An important aspect in the recent development in the physics of TMO is to realize that the combination of these old concepts can produce a variety of interesting and often unexpected phenomena. While these concepts form a basis, a new view point has been established to understand and predict phenomena in a unified way. It is now realized that the strong coupling among charge, spin, and lattice degrees of freedom in TMO are responsible for the rich physics behind and that the key ingredient controlling these strong couplings is the orbital degree of freedom (ODF) [2,11] (see figure 1). The ODF represents the freedom in orbital occupation under various crystal environments for the open shell systems. A typical example where ODF plays a crucial role is $LaMnO_3$ whose ground state is an A-type antiferromagnetic (AF) insulator. (For the definition of various magnetic structures like ferromagnetic (FM), A-, C-, and G-type AF states, refer to figure 2.) The nominal electronic configuration of Mn in $LaMnO_3$ can be expressed as Mn^{3+} ($t^3_{2g\uparrow}e^1_{g\uparrow}$), with the Fermi level lying in the majority spin e_g bands. In the cubic symmetry, two e_g states are degenerate and the half filling of e_g states in $LaMnO_3$ provides us with a typical ODF problem. It is believed that the A–AF ordering of $LaMnO_3$ is accompanied with orbital ordering (OO), which is stabilized by cooperative JT distortion. In this orbital ordered state, two kinds of e_g orbitals, $3x^2 - r^2$ and $3y^2 - r^2$, are alternately occupied at neighbouring Mn^{3+} sites in the ab-plane.

The ODF is important because it can mediate various couplings (see figure 1). For example, it mediates the coupling between structural distortion and magnetism in TMO. Magnetic field directly controls the magnetic ordering, which then affects the OO through hybridization between neighbouring d orbitals. As the lattice is strongly coupled with ODF, magnetic field can indirectly affect the lattice. Conversely magnetic properties can be indirectly controlled by the lattice distortion via ODF. Although magnetism can affect the lattice through the spin–orbit coupling, the above mechanism for the coupling between magnetism and lattice is more pronounced.

One of the reasons why the OO did not play a major role in physics was that the direct experimental observation of the OO used to be difficult. A new experimental technique called anomalous resonant x-ray scattering was recently developed to study the OO and applied to several systems [12]. Nevertheless, it is still argued that the resonant x-ray scattering measures the lattice distortion associated with the OO rather than the OO itself. Under such experimental situations, the first-principles electronic structure calculation serves as a powerful tool in the study of the OO. The usefulness of the method in a variety of environments comes from the combination of several important methodological processes. First, the Car–Parrinello method [13] based on the plane-wave basis provides us with a very accurate way to calculate the total energy and forces, enabling us to optimize the structure. Second, the ultra-soft pseudopotential (PP) scheme [14] makes it possible to treat efficiently the system including hard core elements like oxygen and transition-metal elements. Thirdly, the implementation of iterative diagonalization schemes such as the residual minimization (RMM), direct inversion in the iterative subspace (DIIS) method [15], and the parallelization based on message passing interface (MPI) make the calculations possible even for large systems. In the case of TMO, several other techniques will also be necessary. The extensions to go beyond local density approximation (LDA) and generalized gradient approximation (GGA) [16] are sometimes required, because TMO systems are generally categorized into strongly correlated systems. For this purpose, a technique called LDA + U [17] can provide us with help, particularly for insulating systems. In the LDA + U formalism, the strong correlation between localized electrons is explicitly taken into account through the screened effective on-site electron–electron interaction U^{eff}. To take account of the doping effect without using supercell, the virtual crystal approximation (VCA) will be useful, in which the doped system is simulated with a virtual crystal consisting of virtual atoms whose definition will be given later. All the above techniques are included in the code called STATE (simulational tool for atom technology), which has been used extensively in our studies.

We have been working on the TMO systems extensively in recent years. Examples are FeO and MnO [18, 19], $La_{1-x}Sr_xMnO_3$ [20], $Ca_{2-x}Sr_xRuO_4$ [21, 22], Sr_2FeMO_6 (M = Mo, W and Re) [23], and $SrTiO_3$ [24]. In this article, we will discuss three examples to show the strong coupling between the structural distortion and magnetism mediated by ODF. First, we will demonstrate that the magnetic states in $La_{1-x}Sr_xMnO_3$ can be actually controlled by the lattice distortion via ODF. Second, we will discuss the magnetic and structural properties of ruthenates for both the bulk and the surfaces. Finally, we will discuss the oxygen vacancy effects on the surface of $SrTiO_3$.

2. Methodology

2.1. STATE code

Most of our calculations were done by using our STATE code, which has been carefully designed so that particular efficiency can be achieved for TMO systems. The basic

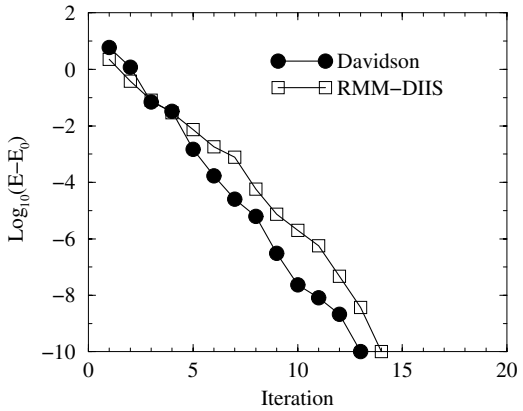

Figure 3. A demonstration for the convergence of self-consistent calculations by using the STATE code. We use the FM cubic perovskite $La_{0.5}Sr_{0.5}MnO_3$ as an example.

methodology employed in the code is the standard first-principles method based on the plane-wave PP method. The particularity of STATE comes from the combination of the following techniques.

(i) We use the ultra-soft PP [14] technique to reduce the cutoff energy required for the wave-function expansion. It is generally true that this technique can reduce the cutoff energy by a factor of 2–3, compared with the norm-conserving PP [25].
(ii) We use the linear tetrahedron method with the curvature correction [26] for the reciprocal space integration. The shift of sampling k-points is allowed so that further reduction of computational efforts can be achieved.
(iii) For the iterative diagonalization of the Kohn–Sham Hamiltonian, two basic schemes were adopted. They are the block-Davidson scheme (DAV) [27] and the RMM-DIIS method [15]. The DAV method is a very accurate and useful scheme when convergence is hard to achieve with other methods, although it is not so efficient for large systems. It can usually be used as a reference scheme, or be used for small systems. The RMM-DIIS method is an efficient method especially suitable for large systems.
(iv) We implemented the LDA + U method in our STATE code so that we can treat some strongly correlated systems for which both LSDA and GGA fail in describing their ground state properties.
(v) We implemented VCA to treat the systems with doping.
(vi) The STATE code is fully parallelized by MPI. Tests have been done for various super computers.

As the techniques (i)–(iii) and (vi) are standard nowadays, in the following subsections we will mostly concentrate on the details of (iv) and (v) in STATE. Finally, to just demonstrate the efficiency of STATE, in figure 3 we show the convergence of self-consistent calculations for the FM cubic perovskite $La_{0.5}Sr_{0.5}MnO_3$, which is a typical example of CMR materials. It is clear that both the DAV method and the RMM-DIIS method achieve very fast convergence.

2.2. LDA + U method in plane-wave pseudopotential scheme

In the LDA + U method, the Coulomb interaction between electrons is explicitly taken into account in the subspace of localized orbitals. The implementation of the LDA + U method in

the plane-wave PP scheme was given in [28]. Here we will give explicit expressions for the case where the $U^{\rm eff}$ parameter may depend not only on the kind of atoms but also on orbitals of the same atom. Following the prescription given in [28], the total energy $E^{\rm LDA+U}$ is given by the corresponding LDA total energy $E^{\rm LDA}$ plus the Hubbard-like interaction energy $E^{\rm U}$ between the localized electrons with subtraction of the double counting part $E^{\rm dc}$,

$$\begin{aligned} E^{\rm LDA+U}[\rho^\sigma, n^\sigma_{I,m}] &= E^{\rm LDA}[\rho^\sigma] + E^{\rm U}[n^\sigma_{I,m}] - E^{\rm dc}[N^\sigma_I] \\ &= E^{\rm LDA}[\rho^\sigma] + \tfrac{1}{2}\left\{ \sum_{I,m,\sigma} U^{\rm eff}_{I,m}(n^\sigma_{I,m} - n^\sigma_{I,m} n^\sigma_{I,m}) \right\} \end{aligned} \tag{1}$$

where ρ^σ is the charge density of the Kohn–Sham states with spin σ and $n^\sigma_{I,m}$ are occupation numbers for the localized orbitals, which are obtained by diagonalizing the density matrix defined for the localized orbitals. I, m and σ are the indexes for atom, orbital and spin, respectively. $N_I = \sum_{m,\sigma} n^\sigma_{I,m}$ is the total number of electrons for the occupied local orbitals on atom I.

The Kohn–Sham equation in the LDA + U scheme is then given by,

$$\hat{H}^{\rm LDA+U}|\Psi^\sigma_{k,i}\rangle = \varepsilon^\sigma_{k,i}\hat{S}|\Psi^\sigma_{k,i}\rangle \tag{2}$$

with

$$\hat{H}^{\rm LDA+U} = \hat{H}^{\rm LDA} + \sum_{I,m} U^{\rm eff}_{I,m}\left(\frac{1}{2} - n^\sigma_{I,m}\right)\frac{\delta n^\sigma_{I,m}}{\delta f^\sigma_{k,i}\Psi^{\sigma *}_{k,i}} \tag{3}$$

where $\Psi^\sigma_{k,i}$ is the self-consistent Kohn–Sham wavefunction, $\varepsilon^\sigma_{k,i}$ is the corresponding eigenenergy, and $f^\sigma_{k,i}$ is its occupation number. k and i are indexes for the wave numbers and bands respectively. $\hat{S}$ is the Hermitian overlap operator as defined in the ultra-soft PP formalism.

Ambiguity exists in the choice of localized orbitals, especially in the case of using the plane-wave basis method. For those methods based on the local basis like LMTO (linear-muffin-tin orbital), it is natural to use the basis orbitals as the localized orbitals. However, in the plane-wave basis method, the definition of localized orbital is nontrivial. Following the idea in [28], a truncated pseudo-atomic wavefunction is chosen as the localized orbital to which $U^{\rm eff}$ is applied. In this sense, the definition is a bit artificial and the localized orbitals depend on the choice of parameters for truncation. However, the pseudo-atomic wavefunctions are obtained in the atomic calculation and do not depend on the crystal structure.

The LDA + U approach described above provides us with a useful and simple way to study strongly correlated systems, although it is semi-empirical in principle. A crucial problem in the practical LDA + U calculations is the choice of $U^{\rm eff}$. Generally two ways are followed to estimate $U^{\rm eff}$. First, $U^{\rm eff}$ can be directly calculated by using the constrained LDA method [29]. However, it is not so meaningful to take this approach in the plane-wave method because of some arbitrariness in the definition of localized orbitals. The second way is to adjust $U^{\rm eff}$ so as to fit the calculated band gap with an experimental one[4]. The second approach is mostly adopted in our PP calculations. We want to comment on one point here. In our LDA + U method based on the plane-wave expansion, because the $U^{\rm eff}$ is nonzero only in a limited (relatively small) region in real space, its actual value is usually larger than the estimation made by another method like LMTO. As an example, in figure 4, we show the calculated band gap as a function of $U^{\rm eff}$ for $SrTiO_3$. Comparing with experimental data, we obtained an estimation of $U^{\rm eff} \sim 7.0$ eV.

[4] In the LDA + U method, the way of subtracting the double counting term is also not unique. The prescription adopted in [17] has some analogy with Slater's transition state as can be also seen in equation (3). This is a reason for using the band gap as a guide to estimate $U_{\rm eff}$.

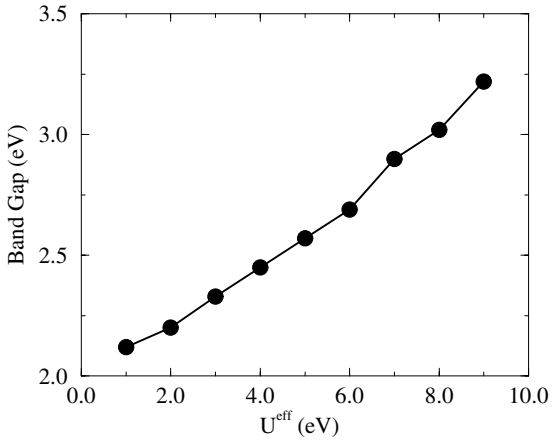

Figure 4. The calculated band gap in LDA + U method as a function of U^{eff} for $SrTiO_3$. The experimental band gap is about 3.2 eV.

2.3. Virtual crystal approximation (VCA) for TMO

Doping or alloying in TMO has been regarded as a standard way to control the physical properties of series of materials. The general formula for perovskite alloy systems can be expressed as $A_{1-x}A'_xB_{1-y}B'_yO_3$. A-sites are usually occupied by alkaline-earth or lanthanoid elements, while B-sites are mostly occupied by transition-metal elements. There are two standard ways to treat the alloy effects. One is the supercell method and the other is the coherent-potential approximation (CPA) [30] based on the scattering theory. As the supercell method requires a large unit cell and is applicable to some specific concentrations x and y in practice, it is not easy to use this method to study a wide range of concentration. On the other hand, while CPA is applicable to any concentration, the plane-wave technique is not suited to this method. Therefore, we adopt a simpler approximation, i.e., a VCA for the alloy effect on the A-sites. In most cases, the main role of the A-site elements is to donate their valence electrons to the rest of the system and to control the occupation of the d bands of the B-site elements. The valence states of the A-site elements are significantly far above the Fermi level. In such a case, VCA can be a good approximation. On the other hand, the alloy effect on the B-site cannot be treated by such a simple approximation as VCA. Therefore, in the present article, we do not treat the B-site alloy systems. Yet, the PP approach has a nice feature in the VCA as explained below and can treat many important A-site alloy systems.

In the VCA based on the PP, the alloy effects are taken into account by constructing virtual atoms, which have an average PP constructed from the constituents. As PP describes the scattering properties of an atom by treating the valence states as if they are the lowest energy (pseudo-)atomic states, the VCA in this way can be applied to alloys consisting of atoms even in different rows of the periodic table. This is a merit of the PP method compared with the all-electron approach for which the VCA can be applied only to the alloys formed by neighbouring elements in the same row.

To construct the VCA in PP scheme, first we generate the ionic PP $\hat{V}^{\text{PP}}_{\text{ion}}$ by unscreening the screened potential $\hat{V}^{\text{PP}}_{\text{scr}}$,

$$\hat{V}^{\text{PP}}_{\text{ion},\alpha}(r) = \hat{V}^{\text{PP}}_{\text{scr},\alpha}(r) - \int \frac{\rho^{v}_{\alpha}(r')}{|r - r'|}\,\mathrm{d}r' - \mu_{\text{xc}}(\rho^{v}_{\alpha}(r) + \rho^{pc}_{\alpha}(r)) \tag{4}$$

where $\rho(r)$ is the charge density with superscripts v or pc denoting the valence part or the partial core correction part. μ_{xc} is the exchange–correlation potential. The label $\alpha = (a, b, \ldots)$ runs

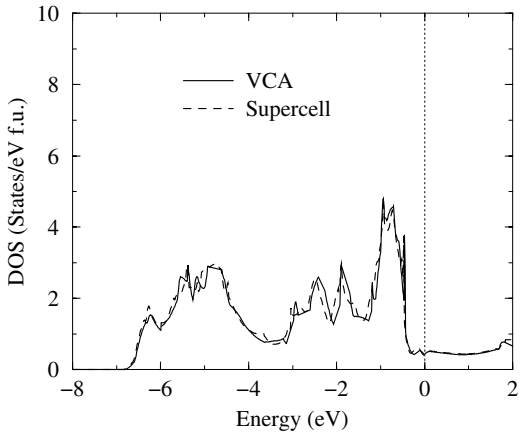

Figure 5. A comparison of calculated electronic DOS for the FM $La_{0.5}Sr_{0.5}MnO_3$ with the cubic structure. The solid curve is for the result obtained by VCA, while the dashed curve gives the result by the supercell calculation.

over all constituent atoms of alloying sites. Here we consider two component alloy systems. The virtual ionic PP can be obtained by mixing the unscreened ionic pseudopotentials,

$$\hat{V}^{\mathrm{PP}}_{\mathrm{ion},x}(r) = x\,\hat{V}^{\mathrm{PP}}_{\mathrm{ion},a}(r) + (1-x)\,\hat{V}^{\mathrm{PP}}_{\mathrm{ion},b}(r) \tag{5}$$

with x denoting the doping ratio. Then we solve the following Schrödinger equation self-consistently for each orbital l to obtain the corresponding pseudo-wavefunction φ_l and eigenvalue ε_l.

$$\left\{T + \hat{V}^{\mathrm{PP}}_{\mathrm{ion},x} + \int \frac{\rho^v_x(r')}{|r-r'|}\,\mathrm{d}r' + \epsilon_{\mathrm{xc}}(\rho^v_x(r) + \rho^{pc}_x(r))\right\}|\varphi_l\rangle = \varepsilon_l|\varphi_l\rangle \tag{6}$$

where T is the kinetic energy operator. The charge density should be obtained self-consistently with the initial charge density given by,

$$\rho^v_x(r) = x\rho^v_a(r) + (1-x)\rho^v_b(r) \tag{7}$$

$$\rho^{pc}_x(r) = x\rho^{pc}_a(r) + (1-x)\rho^{pc}_b(r). \tag{8}$$

Finally, once we obtain the semi-local PP and the corresponding pseudo-wavefunction, we follow the standard step to construct the Kleinman–Bylander type nonlocal PP.

In the above approach, we can use only one projector for each orbital because we need to solve the Schrödinger equation self-consistently instead of getting the wavefunction by inverting the Schrödinger equation with the fixed PP. This is a relatively easy approach, although the restriction of one projector may lead to a little bad transferability.

The validity of our approach for the perovskite TMO systems with A-site alloying has been carefully checked. Both total energy and magnetic exchange parameters have been calculated and compared with supercell calculations. Quite good agreement can be found between them. The calculated electronic structures in the VCA are also in good agreement with those by the supercell calculation. As an example, in figure 5 we show the density of states (DOS) obtained by two approaches for the FM $La_{0.5}Sr_{0.5}MnO_3$ with the cubic perovskite structure. Actually the calculated DOSs in the supercell scheme and in the VCA are almost identical around the Fermi level.

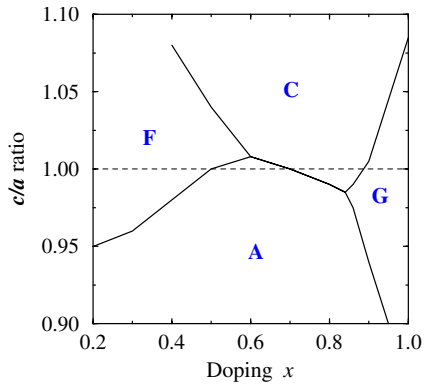

Figure 6. The phase diagram of $La_{1-x}Sr_xMnO_3$ in the plane of c/a and doping x obtained by the total energy calculations [20]. The c/a ratio is varied with the corresponding experimental volume fixed.

3. Examples demonstrating crucial roles of ODF

3.1. ODF-mediated phase control in $La_{1-x}Sr_xMnO_3$

The magnetic ordering can be indirectly controlled by the lattice distortion via ODF. Recently Konishi *et al* [31] succeeded in realizing such control for the CMR manganites $La_{1-x}Sr_xMnO_3$ in the range of $0.3 \leqslant x \leqslant 0.5$ by growing thin films on substrates with some different lattice constants. This is a new way of controlling the phase of manganites through the control of c/a. By changing c/a only from 0.97 to 1.06, the phase of $La_{1-x}Sr_xMnO_3$ takes a sequence of A–AF, FM, C–AF states at around $x = 0.5$. However, except the FM state, experimental assignment of the AF orderings (A-type, C-type and G-type) is indirect and is based on the conjecture by analogy with the well known system $Nd_{1-x}Sr_xMnO_3$ [32].

We will demonstrate that this kind of phase control can be properly predicted by the first-principles calculations [20]. Figure 6 shows the calculated phase diagram obtained by the total energy analysis with GGA [16]. First let us pay attention to the region around $c/a = 1.0$. For the lower doping, the phase diagram is dominated by FM phase; while for the heavy doping, it is dominated by G-type AF phase. However, if we change c/a ratio, two other states, A-type AF and C-type AF, appear and compete with FM and G-type AF states: for $c/a < 1.0$, A-type AF state is stabilized while for $c/a > 1.0$, C-type AF state becomes stable. The theoretical phase diagram agrees quite well with the experimental one. In other words, our theoretical analysis gives a strong support to the experimentalists' conjectures for the AF states.

Here we will mainly discuss the effect of tetragonal distortion of the lattice on the given sequence of magnetic states. For example, if we look at $x = 0.5$, the system will undergo phase transitions from A-type AF state to FM state and to C-type AF state with increasing c/a ratio. We identify two basic mechanisms. First is the OO induced by the lattice distortion as shown in figure 7. Since the e_g bands are antibonding states of O(2p) and Mn(e_g) orbitals, the e_g orbital extending along the elongated Mn–O bond will be preferentially occupied when the tetragonal distortion is set in. Accordingly, the $d_{3z^2-r^2}$ orbitals are more populated than the $d_{x^2-y^2}$ ones for $c/a > 1$ and vice versa for $c/a < 1$. This results in anisotropy of the FM DE interactions: for the less than half-filled majority-spin e_g-bands, the more (less) populated are the orbitals, the stronger (weaker) are the DE interactions among these orbitals. Such anisotropy will favour A–AF and C–AF spin structures for $c/a < 1$ and $c/a > 1$, respectively.

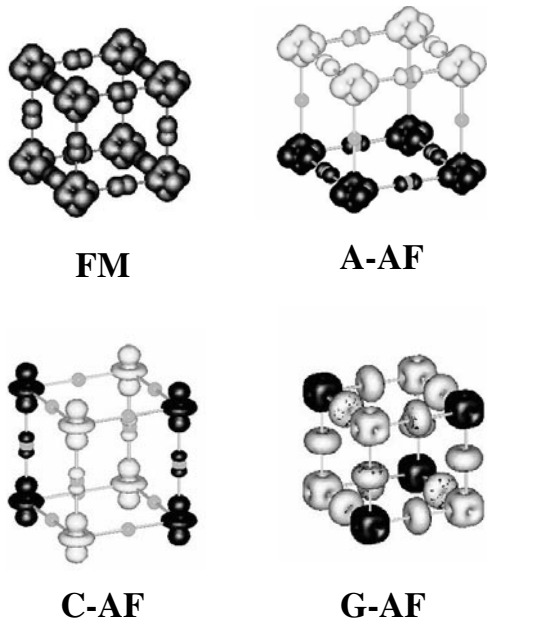

Figure 7. The calculated charge distribution for the energy window with 0.6 eV width just below the Fermi level for different magnetic structures. The different spin components (up and down) are drawn with different grey tones. The Mn atoms sit at the corners of the cube, while oxygen atoms (small spheres) sit at the edge centers.

Another mechanism is related with the distance-dependence of the effective d–d hopping integrals (t) without appealing to the OO and is similar to the bandwidth dependence of nearest neighbour exchange integral J_1 discussed in [33]. By combining the FM–DE and AF SE contributions, J_1 can be expressed as $J_1 = \alpha t - \beta t^2$ with the positively defined parameters α and β. The situation realized in the band structure calculations corresponds to the limit $2t > \alpha/\beta$ and $\partial J_1/\partial t < 0$. Therefore, as t decreases (increases) when the Mn–Mn distance increases (decreases), J_1 is expected to be larger (smaller) in the direction of tetragonal stretching (contraction). This will additionally enhance the tendencies towards A–AF and C–AF spin orderings when $c/a < 1$ and $c/a > 1$, respectively.

3.2. Magnetic phase diagram of $Ca_{2-x}Sr_xRuO_4$

Both the magnetic and the structural instabilities are essential issues for the unconventional superconductivity in Sr_2RuO_4 [22, 34–38], which is the only example of a noncuprate layered perovskite superconductor. It was first suggested that the Sr_2RuO_4 is close to the FM instability [39] with strong FM spin fluctuations, which may naturally lead to a spin-triplet p-wave pairing mechanism [39–42]. However, the recent observation [43] of sizable AF incommensurate spin fluctuation, due to the Fermi surface nesting [44], indicates that more careful studies are needed. As for the structural aspect, it was pointed out by experiments that Sr_2RuO_4 is very close to the structural instability with respect to the RuO_6 rotation [45]. With such a situation, one may consider that three kinds of instabilities, superconducting, magnetic and structural ones, may compete. Nevertheless, the correlation among those instabilities has not been fully discussed. It was found recently [47] that the cleaved surface of this material is reconstructed to form the $c(2 \times 2)$ structure which can be regarded as the frozen RuO_6 rotation mentioned above. This finding turns out to be crucial in the understanding

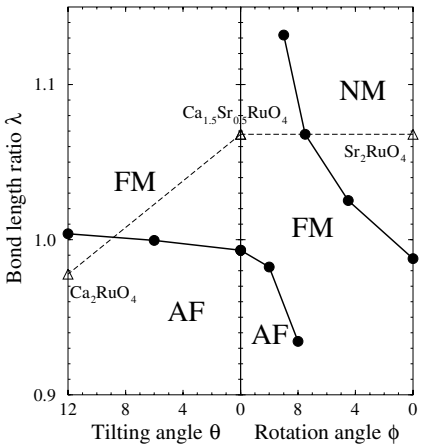

Figure 8. The calculated magnetic phase diagram of $Ca_{2-x}Sr_xRuO_4$ with structural distortions [21]. In the process of tilting RuO_6 octahedron, RuO_6 rotation with 12° is fixed. The solid bold curves denote calculated phase boundaries, while the triangles linked by the dashed line correspond to experimental data.

of the angle-resolved photoemission measurement and has solved the puzzle in the Fermi surface topology [46]. Furthermore, the density-functional calculation predicts that the surface ferromagnetism is strongly stabilized by the structural reconstruction [47]. This prediction suggests that the structural and magnetic instabilities cooperate rather than compete, although the surface ferromagnetism has not been experimentally confirmed up to now.

On the other hand, the recent experimental studies on the very rich phase diagram of $Ca_{2-x}Sr_xRuO_4$ [48] provide us with an opportunity to analyse the correlation between the magnetism and the structure more extensively. With the Ca substitution for Sr, the system is successively driven from the nonmagnetic (NM) two-dimensional (2D) Fermi liquid ($x \sim 2.0$) to a nearly FM metal ($x \sim 0.5$), an antiferromagnetically correlated metal ($0.2 < x < 0.5$), and finally an AF insulator ($x < 0.2$). Since the substitution is isovalent, the dominant effects are the structural modifications due to the reduced ionic size of Ca compared with Sr. (The ionic radii of Ca^{2+} and Sr^{2+} are 1.00 and 1.13 Å, respectively.)

To understand how and why the magnetism of $Ca_{2-x}Sr_xRuO_4$ is affected by structural distortions, and more importantly how the magnetic instabilities are coupled with structural instabilities in Sr_2RuO_4, we calculated a phase diagram of $Ca_{2-x}Sr_xRuO_4$ as shown in figure 8 [21]. The calculations are based on GGA [16]. Our phase diagram can qualitatively explain the experimental one of $Ca_{2-x}Sr_xRuO_4$, demonstrating the crucial roles of structural distortions in the tuning of electronic and magnetic properties, and further supporting our previous prediction for the surface [22]. Our results strongly suggest that, in Sr_2RuO_4, the magnetic fluctuations can be significantly enhanced by the structural fluctuations, implying the necessity of reconsidering the coupling mechanism in the bulk superconductivity.

From right to left of the phase diagram, first the RuO_6 starts to rotate along the c-axis by up to 12°, and then with the 12° rotation being fixed, the RuO_6 starts to tilt up to 12°. The structural analysis by the neutron scattering [49] allows us to make a one-to-one correspondence between the structural changes, i.e. the horizontal axis of our phase diagram, and the doping level x in $Ca_{2-x}Sr_xRuO_4$. Now, the basic tendency suggested by our phase diagram is that the RuO_6 rotation will drive the system from a NM state to a FM state, while the subsequent tilting plus the flattening of RuO_6 will push the system to an AF region. This general tendency is quite consistent with the experimental results. It should be noted that the rich experimental phase

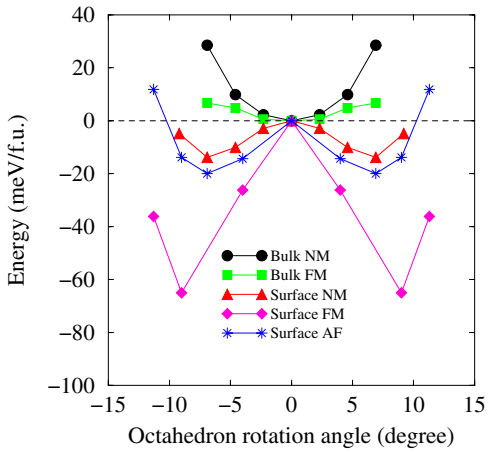

Figure 9. Calculated total energy per formula unit versus octahedron rotation angle for the surface of Sr_2RuO_4 [22]. The curves for different magnetic states are all shifted to make energies of nonrotated structures equal to zero.

diagram can be simply understood in terms of the close coupling between structural distortions and magnetism. Another important aspect in our phase diagram is that the flattening of RuO_6 is so important not only for the AF state but also for the FM state. This suggests that *simply by uniaxial pressure, the Sr_2RuO_4 can be driven from the NM state to a FM state*.

The basic questions concerning our phase diagram are: (1) Why are the RuO_6 rotation and tilting correlated with the tendency to the FM and AF states? (2) Why is the RuO_6 flattening so important for the magnetic solutions? These questions can be understood in terms of the strong coupling between the lattice and the magnetism through the ODF. The RuO_6 rotation couples mostly with the d_{xy} orbital but not with the d_{yz}, d_{zx} orbitals because the pdπ type hybridization between the O(1)-2p and the d_{xy} states will be significantly reduced by the RuO_6 rotation. The direct results of this are, first the narrowing of d_{xy} band width and second the downward shift of d_{xy} band. As the latter brings the van Hove singularity, which is contributed by the d_{xy} orbital, closer to the Fermi level, both of the two results will enhance the DOS at the Fermi level. Once tilting is additionally introduced, all of the t_{2g} bands will become narrower. This will enhance the nesting effect and enhance the AF instability. With the flattening of RuO_6 octahedron, the Ru–O bond length in *ab*-plane will increase, making all the three bands of Ru-t_{2g} states narrower (i.e. making the DOS at the Fermi level higher). This will favour the FM solution. Another very important result of flattening is the orbital polarization. The tetragonal distortion by the flattening will populate the d_{xy} states and depopulate the d_{yz}, d_{zx} states, shifting the nesting vector to the zone boundary. In this sense, flattening may favour the commensurate AF state of the system. Furthermore, if flattening is combined with rotation and tilting, it will induce AF SE by the following mechanism. As was already pointed out, rotation, tilting and flattening of RuO_6 reduce the d band width and populate the d_{xy} orbital preferentially. Therefore, if flattening becomes large enough, the d electron configuration will be $\{d_{xy}\uparrow, d_{yz}\uparrow, d_{zx}\uparrow, d_{xy}\downarrow\}$. Then the hybridization between the occupied $\{d_{yz}\uparrow, d_{zx}\uparrow\}$ orbitals and unoccupied $\{d_{yz}\downarrow, d_{zx}\downarrow\}$ ones will be the source of AF SE. The insulating AF state of Ca_2RuO_4 is realized by such a mechanism.

It is for the same reason that our calculations predict the surface of Sr_2RuO_4 show strong tendency towards FM ground state (see figure 9) [22]. The significant rotation (about 9°) of RuO_6 on the surface was identified by LEED analysis. This rotation will enhance the tendency to the FM state as discussed above.

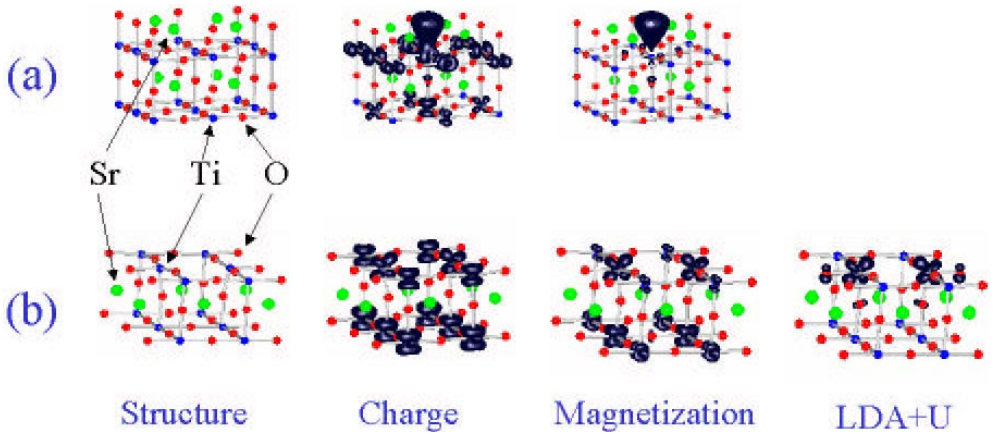

Figure 10. The optimized surface geometry, and the calculated (in GGA) charge and magnetization density distributions around the oxygen vacancy for the energy window of 1.5 eV width just below the Fermi level [24]. The upper row (a) is the case of SrO termination, while the lower one (b) shows that of TiO_2 termination. For TiO_2 termination, the LDA + U ($U^{eff} = 7.0$ eV) result is shown also. In this case, the charge and the magnetization distributions are identical, because only the majority-spin split-off states are available in the energy window.

3.3. Spin and orbital polarization around oxygen vacancy on the surface of $SrTiO_3$

$SrTiO_3$ has been attracting intensive attention over a couple of decades because of the various possible applications. It is widely used in materials science as substrate, due to its very flat surfaces, which can be atomically controlled by chemical treatments [51]. Depending on stoichiometry and structure, the surface of $SrTiO_3$ can be gas sensitive [52], ferroelectric [53–56] and catalytically active [57]. Stoichiometric $SrTiO_3$ (i.e., $Sr^{2+}Ti^{4+}O_3^{2-}$) is an insulator with the Fermi level located within the charge transfer gap between oxygen 2p and Ti 3d states [58]. If the oxygen vacancies exist on the surfaces, part of the Ti 3d states will be occupied and therefore the electronic properties will be modified significantly.

There are several basic questions to be answered for the surface of $SrTiO_3$. First, what is the difference in the electronic structure between SrO and TiO_2 terminated surfaces with oxygen vacancy? Second, the partially occupied transition-metal 3d states are spin-polarized in many cases. Is the local electronic structure induced by oxygen vacancy spin-polarized or not? Thirdly, what are the roles of ODF?

To address all the above questions, we studied the (001) surfaces of $SrTiO_3$ with oxygen vacancies by the first-principles calculations [24]. We first discuss the results obtained by GGA. We found that the partially occupied Ti 3d states show strong spin and orbital polarizations. As for the spin degree of freedom, the FM solution has definitely lower energy than the NM one for both SrO and TiO_2 terminated cases by -99 and -14 meV, respectively, suggesting the strong tendency toward spin-polarization of the defect states. On the other hand, the different orbital pictures around the oxygen vacancy on the SrO and TiO_2 terminated surfaces suggest distinguishable STM images of the two cases. Figure 10 shows the calculated geometry, the charge and spin-polarization distributions around the oxygen vacancy for two terminations. For the SrO terminated surface, the loss of the apical oxygen will mostly affect the Ti site just below the vacancy. In this case, the loss of the strong pd hybridization along the surface normal, taken as z direction, will pull the $d_{3z^2-r^2}$ state which is the pd antibonding state down significantly. The charge distribution shown in figure 10 clearly demonstrates that the occupied Ti 3d states

have strong $d_{3z^2-r^2}$ character. However, the TiO_2 terminated surface is quite different, in the sense that there are two nearest neighbour Ti sites around the oxygen vacancy. The effects of vacancy will be shared by the two neighbouring surface Ti sites. If we take the x axis as the Ti–O bond direction, the partially occupied Ti 3d states are mostly the d_{xz} orbitals. For the perfect TiO_2 terminated surface, the d_{yz} and d_{zx} states, which are degenerate, are lower in energy than the d_{xy} state due to the loss of the $pd\pi$ hybridization with the ligand oxygen from another side of the surface. However, after the formation of the oxygen vacancy, the d_{zx} states at the neighbouring Ti atoms are further lowered due to another loss of the $pd\pi$ hybridization. The ordering in ODF is clearly shown in the charge and magnetization distributions in figure 10. Finally we make some comments on the problems in GGA for the TiO_2-terminated surface and discuss the improvements by the LDA + U method with $U^{\text{eff}} = 7.0$ eV. As was already mentioned this value of U_{eff} is obtained to reproduce the bulk band gap of $SrTiO_3$. In GGA, although the oxygen vacancy produces the spin polarization at the neighbouring Ti sites, the system becomes metallic with the Fermi level lying in both the majority and minority spin Ti d bands. This is inconsistent with the measurement by the scanning tunnelling spectroscopy (STS) [59]. With the LDA + U method, a split-off gap state only for the majority spin appears in the band gap about 1.5 eV below the Fermi level and the system becomes insulating [24].

4. Summary

With all those examples discussed so far, we have demonstrated that the magnetism in TMO is strongly correlated with the structural distortions. By controlling the structural distortion, we can control the magnetic state of the system. Conversely, by controlling the magnetic state of the system, we can affect the structural distortion. We have emphasized that the coupling between magnetism and lattice distortion is mediated by ODF. As the direct experimental observation of the ODF is still not easy, theoretical analysis should play an important role. The recent development of first-principles calculations based on the density-functional theory provides us with a powerful tool to study the physics associated with ODF in TMO.

References

[1] See, for example, Imada M, Fujimori A and Tokura Y 1998 *Rev. Mod. Phys.* **70** 1039
[2] See, for example, Tokura Y (ed) 1999 *Colossal-Magnetoresistive Oxides* (Tokyo: Gordon and Breach)
[3] Salamon M B 2001 *Rev. Mod. Phys.* **73** 583
[4] Maeno Y, Hashimoto H, Yoshida K, Nishizaki S, Fujita T, Bednorz J G and Lichtenberg F 1994 *Nature* **372** 532
[5] Zener C 1951 *Phys. Rev.* **82** 403
Anderson P W and Hasegawa H 1955 *Phys. Rev.* **100** 675
de Gennes P-G 1960 *Phys. Rev.* **118** 141
[6] Anderson P W 1950 *Phys. Rev.* **79** 350
[7] Kanamori J 1960 *J. Appl. Phys.* **31** 14S
[8] Bill H 1984 *Dynamical Jahn–Teller Effect in Localized Systems* ed Yu E Rerlin and M Wager (New York: Elsevier)
[9] Millis A J, Littlewood P B and Shraiman B I 1995 *Phys. Rev. Lett.* **74** 5144
[10] Millis A J, Shraiman B I and Mueller R 1996 *Phys. Rev. Lett.* **77** 175
[11] Tokura Y and Nagaosa N 2000 *Science* **288** 462
[12] Murakami Y *et al* 1998 *Phys. Rev. Lett.* **80** 1932
Murakami Y *et al* 1998 *Phys. Rev. Lett.* **81** 582
[13] Car R and Parrinello M 1985 *Phys. Rev. Lett.* **55** 2471
[14] Vanderbilt D 1990 *Phys. Rev.* B **41** 7892
[15] Kresse G and Furthmüller J 1996 *Comput. Mater. Sci.* **6** 15
[16] Perdew J P, Burke K and Ernzerhof M 1996 *Phys. Rev. Lett.* **77** 3865
[17] Solovyev I V, Dederichs P D and Anisimov V I 1994 *Phys. Rev.* B **50** 16 861

[18] Fang Z, Terakura K, Sawada H, Miyazaki T and Solovyev I 1998 *Phys. Rev. Lett.* **81** 1027
[19] Fang Z, Solovyev I, Sawada H and Terakura K 1999 *Phys. Rev.* B **59** 762
[20] Fang Z, Solovyev I and Terakura K 2000 *Phys. Rev. Lett.* **84** 3169
[21] Fang Z and Terakura K 2001 *Phys. Rev.* B **64** R20 509
[22] Matzdorf R, Fang Z, Ismail, Zhang J, Kimura T, Tokura Y, Terakura K and Plummer E W 2000 *Science* **289** 746
[23] Fang Z, Terakura K and Kanamori J 2001 *Phys. Rev.* B **63** R180407
[24] Fang Z and Terakura K 2000 *Surf. Sci.* **470** L75
[25] Troullier N and Martins J L 1991 *Phys. Rev.* B **43** 1993
[26] Blöchl P E, Jepsen O and Andersen O K 1994 *Phys. Rev.* B **49** 16 223
[27] Davidson E R 1978 *J. Comput. Phys.* **17** 87
Liu B *Report on the Workshop Numerical Algorithms in Chemistry: Algebraic Methods* ed C Moler and I Shavitt p 49
[28] Sawada H, Morikawa Y and Terakura K 1997 *Phys. Rev.* B **56** 12 154
[29] Solovyev I V and Dederichs P H 1994 *Phys. Rev.* B **49** 6736
[30] Soven P 1967 *Phys. Rev.* **156** 809
Taylor D W 1967 *Phys. Rev.* **156** 1017
[31] Konishi Y, Fang Z, Izumi M, Manako T, Kasai M, Kuwahara H, Kawasaki M, Terakura K and Tokura Y 1999 *J. Phys. Soc. Japan* **68** 3790
[32] Kuwahara H, Okuda T, Tomioka Y, Asamitsu A and Tokura Y 1999 *Phys. Rev. Lett.* **82** 4316
[33] Solovyev I V and Terakura K 1999 *Phys. Rev. Lett.* **82** 2959
[34] Imai T, Hunt A W, Thurber K R and Chou F C 1998 *Phys. Rev. Lett.* **81** 3006
[35] Mackenzie A P *et al* 1998 *Phys. Rev. Lett.* **80** 161
Mackenzie A P *et al* 1998 *Phys. Rev. Lett.* **80** 3890
[36] Luke G M *et al* 1998 *Nature* **394** 558
[37] Riseman T M *et al* 1998 *Nature* **396** 242
[38] Laube F *et al* 2000 *Phys. Rev. Lett.* **84** 1595
[39] Rice T M and Sigrist M 1995 *J. Phys.: Condens. Matter* **7** L643
[40] Mazin I I and Singh D J 1997 *Phys. Rev. Lett.* **79** 733
[41] Tewordt L 1999 *Phys. Rev. Lett.* **83** 1007
[42] Ishida K *et al* 1998 *Nature* **396** 658
[43] Sidis Y *et al* 1999 *Phys. Rev. Lett.* **83** 3320
[44] Mazin I I and Singh D J 1999 *Phys. Rev. Lett.* **82** 4324
[45] Braden M and Reichardt W 1998 *Phys. Rev.* B **57** 1236
[46] Damascelli A, Lu D H, Shen K M, Armitage N P, Ronning F, Feng D L, Kim C and Shen Z-X 2000 *Phys. Rev. Lett.* **85** 5194
[47] Matzdorf R *et al* 2000 *Science* **289** 746
[48] Nakatsuji S and Maeno Y 2000 *Phys. Rev. Lett.* **84** 2666
Nakatsuji S and Maeno Y 2000 *Phys. Rev.* B **62** 6458
[49] Friedt O *et al* 2000 *Preprint* cond-mat/0007218
[50] Mazin I I and Singh D J 1997 *Phys. Rev.* B **56** 2556
[51] Kawasaki M, Takahashi K, Maeda T, Tsuchiya R, Shinohara M, Ishiyama O, Yonazawa T, Yoshimoto M and Koinuma H 1994 *Science* **266** 1540
[52] Bieger T, Maier J and Waser R 1992 *Sensors. Actuators* B **7** 763
[53] Ravikumar V, Wolf D and Dravid V P 1995 *Phys. Rev. Lett.* **74** 960
[54] Zhong W and Vanderbilt D 1995 *Phys. Rev. Lett.* **74** 2587
[55] Itoh M, Wang R, Inaguma Y, Yamaguchi T, Shan Y and Nakamura T 1999 *Phys. Rev. Lett.* **82** 3540
[56] Bichel N, Schmidt G, Heinz K and Müller K 1989 *Phys. Rev. Lett.* **62** 2009
[57] Mavroides J G, Kafalas J A and Kolisar D F 1976 *Appl. Phys. Lett.* **28** 241
[58] Cardona M 1965 *Phys. Rev.* A **651** 140
[59] Tanaka H, Matsumoto T, Kawai T and Kawai S 1993 *Japan. J. Appl. Phys.* **32** 1405